Nonlocal effects in gyrokinetic turbulence simulations using GENE

2010 J. Phys.: Conf. Ser. 260 012011

(http://iopscience.iop.org/1742-6596/260/1/012011)

Journal of Physics: Conference Series **260** (2010) 012011 doi:10.1088/1742-6596/260/1/012011

Nonlocal effects in gyrokinetic turbulence simulations using GENE

T Görler[1], X Lapillonne[2], S Brunner[2], J Chowdhury[3], T Dannert[4], F Jenko[1], B F McMillan[2], F Merz[1], D Told[1] and L Villard[2]

[1] Max-Planck-Institut für Plasmaphysik, IPP-EURATOM Association, Garching, Germany
[2] École Polytechnique Fédérale de Lausanne, Centre de Recherches en Physique des Plasmas, Association Euratom-Confédération Suisse, CH-1015 Lausanne, Switzerland
[3] Institute for Plasma Research, Bhat, Gandhinagar - 382 428, India
[4] Rechenzentrum der Max-Planck-Gesellschaft und des Max-Planck-Institutes für Plasmaphysik, EURATOM Association, D-85748, Germany

E-mail: tobias.goerler@ipp.mpg.de

Abstract. Modeling of anomalous transport, typically based on gyrokinetic theory, is an essential tool for better understanding and possibly improving the confinement of magnetic fusion plasmas. A well-benchmarked and established implementation of the gyrokinetic Vlasov-Maxwell system of equations can, for instance, be found in the software package GENE. This Eulerian code has recently been enhanced to optionally consider full radial temperature, density, and geometry variations allowing for investigations of nonlocal effects instead of using the radially local flux-tube approximation. First investigations on the importance of finite-size effects are presented and compared with results from the gyrokinetic Lagrangian PIC code ORB5 [S. Jolliet *et al.* 2007 *Comput. Phys. Commun.* **177** 409, B.F. McMillan *et al.* 2008 *Phys. Plasmas* **15** 052308]. Special attention is drawn to a specific nonlocal effect, namely heat flux avalanches.

1. Introduction

The thorough understanding and reliable prediction of the so-called anomalous transport of heat, momentum, and particles across the magnetic surfaces (hereafter referred to as the radial direction) is one of the key physical problems on the way to efficient fusion power plants based on toroidal magnetic confinement. By now, this effect is commonly attributed to small-scale (roughly comparable to the ion or electron gyroradius), low-frequency (much smaller than the ion and electron gyrofrequency) turbulence driven by microinstabilities which extract free energy from the background temperature and density gradients. An appropriate theoretical framework for high-temperature, low-density and thus weakly collisional fusion plasmas is provided by the gyrokinetic approach [1, 2] where fast dynamics (e.g., the particle gyromotion) are eliminated from the full kinetic description but low-frequency physics is kept. In general, the resulting gyrokinetic Vlasov-Maxwell system of equations in five-dimensional phase space can only be solved numerically. Existing implementations can be classified into so-called local and global codes. The former typically employ a specific flux-tube simulation domain [3, 4, 5] which is restricted to a narrow box perpendicular to the magnetic field lines. Consequently, temperature and density profiles and their gradients are just evaluated at the (radial) center position of this domain and periodic boundary conditions allowing for the application of fast and efficient spectral methods are employed. In this case, however, one implicitly assumes a gyro-Bohm

transport scaling, i.e. a Bohm scaling reduced by the gyroradius-to-machine-size ratio ρ^* where the latter has to be small. Investigations on the limit of such assumed scalings and applications to small fusion devices thus have to rely on global codes where full radial temperature, density and geometry profiles are considered. Amongst others, an implementation of both approaches can be found in the software package GENE [6, 7, 8, 9] which is a massively parallelized, comprehensive Eulerian δf code. In this paper, we present comparisons of the recently developed global version with the well-established local code version and the global gyrokinetic Lagrangian PIC code ORB5 [10, 11] and hereby study the role of finite-size effects.

2. Code description

In gyrokinetic theory, a gyrocenter distribution function f_σ per species σ with mass m_σ and charge q_σ is evolved in time using an accordingly transformed Vlasov equation (or Boltzmann equation if weak collisions are considered) which reads in advection form [1]

$$\frac{\partial f_\sigma}{\partial t} + \dot{\mathbf{X}} \cdot \nabla f_\sigma + \dot{v}_\parallel \frac{\partial f_\sigma}{\partial v_\parallel} + \dot{\mu} \frac{\partial f_\sigma}{\partial \mu} = 0 \tag{1}$$

where the magnetic moment is an adiabatic invariant fulfilling $\dot{\mu} = 0$. The time derivatives of the gyrocenter coordinate $\mathbf{X}$ and the parallel velocity $v_\parallel$ are given in the low-β limit (small thermal pressure compared to the magnetic pressure) by

$$\dot{\mathbf{X}} = v_\parallel \hat{\mathbf{b}}_0 + \frac{B_0}{B_{0\parallel}^*} \left(\mathbf{v}_{\bar{\chi}} + \mathbf{v}_{\nabla B} + \mathbf{v}_c \right) \qquad \text{and} \qquad \dot{v}_\parallel = -\frac{\dot{\mathbf{X}}}{m_\sigma v_\parallel} \cdot \left(q_\sigma \nabla \bar{\phi}_1 + \frac{q_\sigma}{c} \hat{\mathbf{b}}_0 \dot{\bar{A}}_{1\parallel} + \mu \nabla B_0 \right).$$

Here, B_0 denotes the modulus of the magnetic (background) field vector $\mathbf{B}_0$, $\hat{\mathbf{b}}_0 = \mathbf{B}_0/B_0$ the corresponding unit vector, $B_{0\parallel}^* = \hat{\mathbf{b}}_0 \cdot \mathbf{B}_0^*$ the parallel component of $\mathbf{B}_0^* = \nabla \times (\mathbf{A}_0 + \frac{m_\sigma c}{q_\sigma} v_\parallel \hat{\mathbf{b}}_0)$, and $\bar{\chi}_1 = \bar{\phi}_1 - \frac{v_\parallel}{c} \bar{A}_{1\parallel}$ the gyroaveraged scalar potential in the gyrocenter moving frame with the fluctuating fractions of the electrostatic potential ϕ_1 and the parallel vector field component $A_{1\parallel}$. The total drift velocity consists of the generalized $\mathbf{E} \times \mathbf{B}$ velocity $\mathbf{v}_{\bar{\chi}} = \frac{c}{B_0} \hat{\mathbf{b}}_0 \times \nabla \bar{\chi}_1$, the gradient-B velocity $\mathbf{v}_{\nabla B_0} = \frac{\mu c}{q_\sigma B_0} \hat{\mathbf{b}}_0 \times \nabla B_0$, and the curvature drift velocity $\mathbf{v}_c = \frac{m_\sigma c}{q_\sigma B_0} v_\parallel^2 \hat{\mathbf{b}}_0 \times \frac{\nabla B_0}{B_0}$. Overbars and $\langle \ldots \rangle$ brackets denote gyroaverages being defined as $\bar{\phi}_1(\mathbf{X}) \equiv \mathcal{G}\left[\phi_1(\mathbf{X})\right] \equiv \frac{1}{2\pi} \oint \mathrm{d}\theta \; \phi_1(\mathbf{X} + \mathbf{r}(\theta))$ with the gyroradius vector $\mathbf{r}(\theta)$ being orthogonal to the magnetic field.
In the following, a δf splitting is employed, i.e. the fluctuating part f_1 of the distribution function is considered to be small compared to the stationary background part f_0 – here, chosen to be a local Maxwellian – such that the gyrokinetic Vlasov equation can be rewritten and simplified. Keeping only first order terms in the perturbation parameter expansion, the $\nabla\chi \times \mathbf{B}$ nonlinearity is retained while higher-order terms like the so-called $v_\parallel$-nonlinearity are neglected. This is in line with careful studies in Refs. [12, 13, 14]. The distribution functions for the different species are coupled in the low-β approximation through the gyrokinetic Poisson equation and the parallel component of Ampère's law. The former reads

$$-\nabla_\perp^2 \phi_1 = 4\pi \sum_\sigma \left(q_\sigma \bar{n}_{1\sigma} + n_{0\sigma} \frac{q_\sigma^2}{T_{0\sigma}} \left[\frac{B_0}{T_{0\sigma}} \int \langle \bar{\phi}_1(\mathbf{x} - \mathbf{r}) \rangle \mathrm{e}^{-\frac{\mu B_0}{T_{0\sigma}}} \mathrm{d}\mu - \phi_1(\mathbf{x}) \right] \right) \tag{2}$$

where the gyrocenter density is $\bar{n}_{1\sigma} = \frac{2\pi}{m_\sigma} \iint B_{0\parallel}^* \langle f_{1\sigma}(\mathbf{x} - \mathbf{r}) \rangle \mathrm{d}v_\parallel \mathrm{d}\mu$. If adiabatic electrons are assumed, the electron contribution on the right hand side of Eq. (2) is replaced by $n_{1e} = \frac{e n_{0e}}{T_{0e}} (\phi_1 - \langle \phi_1 \rangle_{\mathrm{FS}})$, with $\langle \ldots \rangle_{\mathrm{FS}}$ indicating a flux surface average. Note, that derivatives of equilibrium quantities are here ordered small (as before). The second field equation is

$$-\nabla_\perp^2 A_{1\parallel} = \frac{4\pi^2 B_0}{c} \sum_\sigma q_\sigma \iint \langle f_{1\sigma}(\mathbf{x} - \mathbf{r}) \rangle v_\parallel \mathrm{d}v_\parallel \mathrm{d}\mu. \tag{3}$$

In GENE, Eqs. (1)-(3) are evaluated in the first order perturbation expansion using a field-aligned coordinate system in order to take advantage of the strong anisotropy of plasma turbulence itself. Hence, just a few (on the order of several 10) grid points are required in the direction along the field line where turbulent structures hardly vary. As mentioned earlier, local codes typically employ the flux tube concept where periodic boundary conditions can be taken in both directions (x, y) perpendicular to the magnetic field. In the parallel (z) direction quasi-periodic boundary conditions are implemented which account for the stretching of the simulation box due to magnetic shear. They are also adopted in the global version of GENE. However, in the latter, the radial box size is significantly enhanced to a large fraction of the minor radius and periodic boundary conditions are inapplicable since full radial profiles, e.g. of temperatures and densities are considered. Consequently, (pseudo-) spectral methods can only be employed in the binormal (y) direction. One major consequence is that gyroaverage operators, for instance, cannot be given a simple analytic form as in the (k_x, k_y) Fourier space. Hence, the integration over gyroangles has to be performed using interpolation techniques in real space for the radial direction. In GENE, the latter is realized using finite element interpolation which effectively amounts to a Hermite polynomial interpolation, for details see [9].

Besides hyper diffusion terms and a simple Krook operator, $\mathrm{d}f_{1\sigma}/\mathrm{d}t = -S_{\mathrm{Krook}} f_{1\sigma}$, which can be added close to the radial boundaries to create artificial buffer zones where fluctuations are damped, two further sources/sinks are available in GENE. On the one hand, an artificial Krook-type heat source term similar to the model in Ref. [11],

$$\mathcal{S}_K(x, |v_\parallel|, \mu) = -\gamma_h \left[\langle f_{1\sigma}(\mathbf{X}, |v_\parallel|, \mu)\rangle_{\mathrm{FS}} - \langle f_{0\sigma}(\mathbf{X}, |v_\parallel|, \mu)\rangle_{\mathrm{FS}} \frac{\langle \int d\mathbf{v}\ \langle f_{1\sigma}(\mathbf{X}, |v_\parallel|, \mu)\rangle_{\mathrm{FS}}\rangle_{\mathrm{FS}}}{\langle \int d\mathbf{v}\ \langle f_{0\sigma}(\mathbf{X}, v_\parallel, \mu)\rangle_{\mathrm{FS}}\rangle_{\mathrm{FS}}} \right], \tag{4}$$

with $f_{1\sigma}(\mathbf{X}, |v_\parallel|, \mu) = (f_{1\sigma}(\mathbf{X}, v_\parallel, \mu) + f_{1\sigma}(\mathbf{X}, -v_\parallel, \mu))/2$, is added to the right hand side of the Vlasov equation. Being applied over the whole radial simulation domain, it is designed to fix the temperature profile on average, while conserving the flux-surface averaged density and parallel momentum. Alternatively, a localized heat source model closely following the implementation being described in Ref. [15] can be used. In normalized units, it is added to the right hand side of the Vlasov equation as $\frac{\mathrm{d}f_1}{\mathrm{d}t} = \mathcal{S}_H = \mathcal{S}_0 \mathcal{S}_x \mathcal{S}_E$ with

$$\mathcal{S}_E = \frac{2}{3} \frac{1}{p_{0\sigma}(x)} \left(\frac{v_\parallel^2 + \mu B_0}{T_{0\sigma}(x)/T_{0\sigma}(x_0)} - \frac{3}{2} \right) f_{0\sigma}, \qquad \mathcal{S}_x = \mathcal{S}_{x,in}(x) \,/ \int \mathrm{d}^3x\, \mathcal{S}_{x,in}(x) J(x, z), \tag{5}$$

and the source amplitude $\mathcal{S}_0$. Here, $J(x, z)$ denotes the configuration space Jacobian and $\mathcal{S}_{x,in}(\hat{x})$ is a user-defined radial source profile.

3. Linear GENE results

Since GENE offers the possibility to run simulations in the global as well as in the local mode, using pseudo-spectral methods in the radial direction in the latter case, it is obvious to take this inherent advantage for two reasons. Firstly, both approaches should produce similar results in the small $\rho^* = \rho_s/a$ (with the Tokamak minor radius a) limit which can be used as a test for the implementation of the (different) numerical schemes. Secondly, it becomes possible to gain some first insights on the range of ρ^* values where finite-size effects become important. In this section, we present corresponding linear simulation results.

Here, the temperature and density profile shapes for the global simulations are either chosen to exhibit peaked logarithmic gradient profiles by considering

$$(T_\sigma, n_\sigma) = (T_{\mathrm{ref}}, n_{\mathrm{ref}}) \exp\left[-\kappa_{(T_\sigma, n_\sigma)} \varepsilon \Delta(T, n) \tanh\left(\frac{(x - x_0)/a}{\Delta(T, n)} \right) \right], \tag{6}$$

or flat top gradient profiles by choosing

$$(T_\sigma, n_\sigma) = (T_{\mathrm{ref}}, n_{\mathrm{ref}}) \left[\frac{\cosh\left(\frac{(x-x_0)/a+\delta(T,n)}{\Delta(T,n)}\right)}{\cosh\left(\frac{(x-x_0)/a-\delta(T,n)}{\Delta(T,n)}\right)} \right]^{-\kappa_{(T_\sigma,n_\sigma)}\,\varepsilon\,\Delta(T,n)/2} . \tag{7}$$

In definitions (6) and (7), T_{ref} and n_{ref} denote reference temperatures and densities at the center position x_0 (here, $x_0 = 0.5a$). Furthermore, $\delta(T,n)$ and $\Delta(T,n)$ are characteristic gradient profile widths, which will be varied while $\kappa_T = \max(R_0/L_T)$ and $\kappa_n = \max(R_0/L_n)$ denote the maximum temperature and density gradient values and ε is the inverse aspect ratio between minor radius a and major radius R_0. If not stated otherwise, these values will be chosen as in the Cyclone Base Case (CBC) [16] parameter set, i.e. $\kappa_T = 6.96$, $\kappa_n = 2.23$ and $\varepsilon = 0.36$. The shape of the flux surfaces is assumed to be circular and concentric such that x can be identified with the minor radius r of each flux surface (see Ref. [17] for details). The safety factor profile is $q(x/a) = 0.498(x/a)^4 - 0.466(x/a)^3 + 2.373(x/a)^2 + 0.854$ where the center values of $q_0 = q(x_0) = 1.42$ and shear $\hat{s}_0 = \hat{s}(x_0) = 0.8$ match the CBC values. In a first step, the radial simulation box length l_x is kept fixed with respect to the ion gyroradius $\rho_i = \rho_s$. Hence, with decreasing ρ^* parameter, it becomes smaller and smaller compared to the minor radius a so that eventually only a very narrow region about a central flux surface at $x/a = 0.5$ is taken into account. Naturally, such simulations should converge towards those performed with the local code if periodic boundary conditions are assumed. The resulting growth rates using adiabatic electrons with $T_e = T_i$ are presented in Fig. 1. Note that each simulation has been performed at

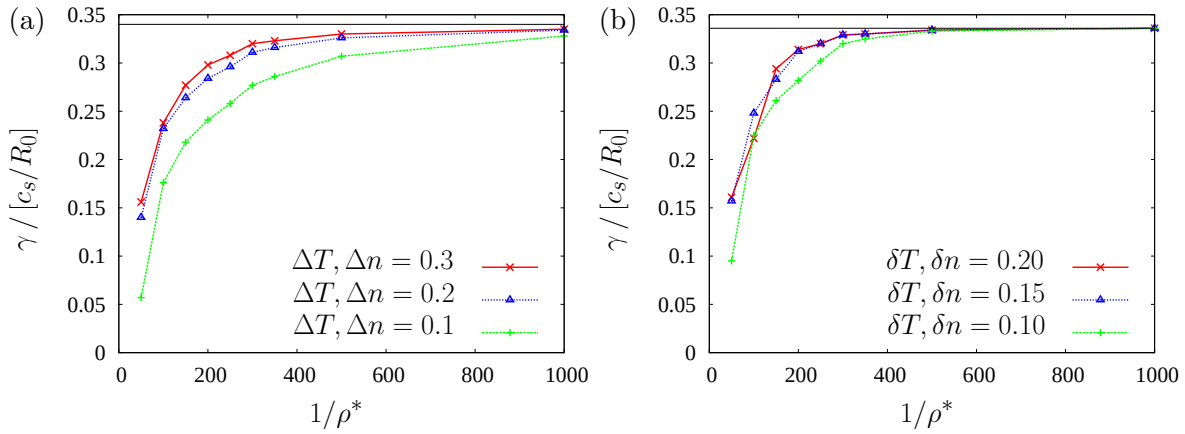

Figure 1. Growth rate of an ITG mode with adiabatic electrons for $k_y\rho_s \approx 0.3$ as function of the inverse ρ^* value using (a) the peaked and (b) the flat temperature and density gradient profiles. The latter are additionally employing $\Delta T, \Delta n = 0.025$ as second characteristic width. Here, the radial simulation box length is kept fixed with respect to the gyroradius. The local code result considering the maximum gradient at x_0 is shown as thin, black line.

the wave number being closest to $k_y\rho_s = 0.3$. The exact value cannot be chosen in general since the box size in the y direction is constrained by the torus dimensions. For details on this issue and on the chosen numerical parameters, see Ref. [18]. The resulting deviations tend to be larger with increasing ρ^* values which explains the jagged behavior in this region. All in all, a very good agreement with the local result can be observed for different profiles and widths at small ρ^*. However, with increasing value of ρ^*, the global code results start to deviate from the local results depending on the profile shape. Here, the broader logarithmic gradient profile shape, Eq. (7) sticks longer to the local result than the narrow one, Eq. (6), which can be attributed to a larger effective (radial) drive region. Further simulation results using a different physical scenario –

namely, an ITG-Kinetic Ballooning (Alfvénic ITG) Mode transition with gyrokinetically treated electrons (with true proton-electron mass ratio) and electromagnetic fluctuations – are shown in Fig. 2. For these runs, the peaked logarithmic gradient profile, Eq. (6), has been employed

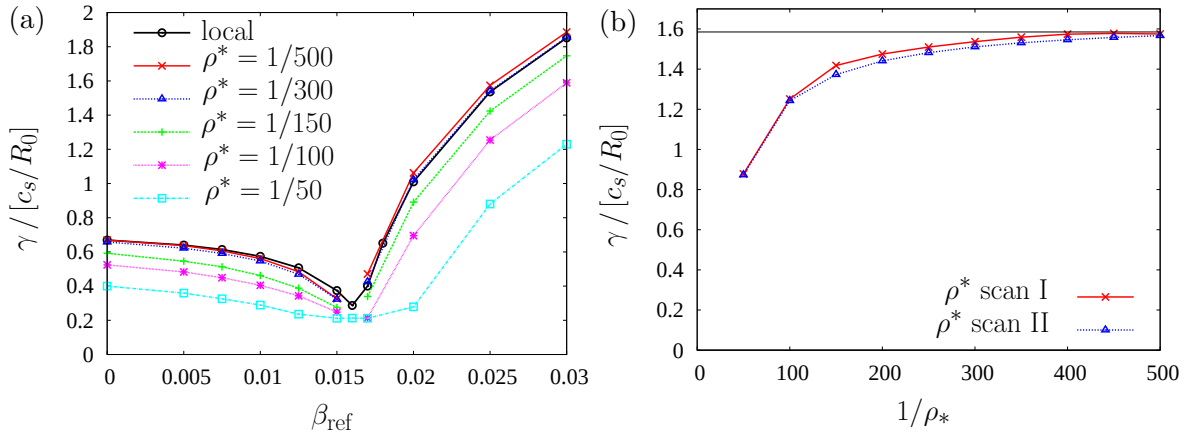

Figure 2. (a) Growth rate at $k_y\rho_s \approx 0.284$ as function of $\beta_{\rm ref}$ and parametrized by different values of ρ^* together with the local code result. (b) Growth rate at the same binormal wave number but fixed $\beta_{\rm ref} = 2.5\%$ as function of the inverse ρ^* value. Here, the radial simulation box is kept fixed with respect to (I) the gyroradius and (II) the minor radius. The local code result using the maximum gradients is again shown as thin, black line. The ideal MHD ballooning mode threshold approximately evaluates to $\beta_{\rm ref} \approx 1.6\%$.

with fixed $\Delta T, \Delta n = 0.3$. The left plot still considers l_x/ρ_s =const. and contains the linear growth rate for different values of ρ^* and $\beta_{\rm ref} = 8\pi p_{\rm ref}/B^2_{\rm ref}$ with reference pressure $p_{\rm ref}$ and magnetic field $B_{\rm ref}$. Obviously, the previously observed convergence behavior seems to hold even for a wide range of $\beta_{\rm ref}$ values since the global growth rates do well agree with the local ones for $\rho^* \lesssim 1/300$. A comparison with a different kind of ρ^* scan is presented in fig. 2(b) for a fixed $\beta_{\rm ref}$ value of 2.5%. Here, the box size is kept fixed with respect to the minor radius a so that more and more radial grid points are required to resolve the mode structures with decreasing gyroradius-to-machine-size ratio. In this case, only minor deviations, i.e. a slightly slower convergence towards the local limit, can be observed. However, if the mode structures exhibit a significantly large ballooning angle – i.e. a finite k_x wave number, respectively – the growth rates in the small ρ^* limit might appear to be systematically below the local code results (see, e.g., Ref. [18]). As is discussed in Ref. [19, 20] in more detail, this can be linked to the radial mode structure in relation to the radial width of the linearly unstable region.

4. Nonlinear GENE and ORB5 results

Since the prediction of heat and particle diffusivities is the true motivation for performing gyrokinetic simulations, it is now most interesting to study the nonlinear physics and the underlying transport scaling. Although this task has already been tackled in the past [21, 22], no coherent picture has evolved so far due to inconsistent findings. In the following, we present results of nonlinear gyrokinetic simulations using adiabatic electrons with $T_e = T_i$ for different values of ρ^* gained from GENE and the Lagrangian PIC code ORB5 [10, 11]. Here, the Krook-type heat sources have been applied in order to approximately maintain the average profiles

$$R_0 \frac{\mathrm{d}\ln(T_i, n)}{\mathrm{d}x} = \kappa_{(T_i,n)} \left[1 - \cosh^{-2}\left(\frac{x - x_0 - \delta/2}{a\Delta} \right) - \cosh^{-2}\left(\frac{x - x_0 + \delta/2}{a\Delta} \right) \right] \qquad (8)$$

taken for $|x - x_0| \leq \delta/2$ and zero otherwise with $\delta = 0.8a$, $\Delta = 0.04$, $x_0 = a/2$, and the maximum logarithmic gradient lengths $\kappa_n = 2.2$ and $\kappa_{T_i} = 7.1$ and 7.5. The latter is indeed set

to these two different initial values in order to allow for a linear interpolation of the time-averaged heat diffusivities at the CBC value of $\kappa_{T_i} = 6.96$ in the quasi-stationary saturation phase where the initial temperature profiles are relaxed by some amount but still clearly above the nonlinear threshold. Again, the flux surfaces are assumed to be circular concentric with a safety factor profile of $q(x) = 0.85 - 0.01x/a + 2.28(x/a)^2 - 0.09(x/a)^3 + 0.22(x/a)^4$. Further details, e.g. on the numerical parameters, can be found in Refs. [20, 23]. The resulting ρ^* dependencies of the ion heat diffusivity measured in units of $\chi_{\mathrm{GB}} = \rho_s^2 c_s/a$ are shown in Fig. 3(b). First of all, both codes

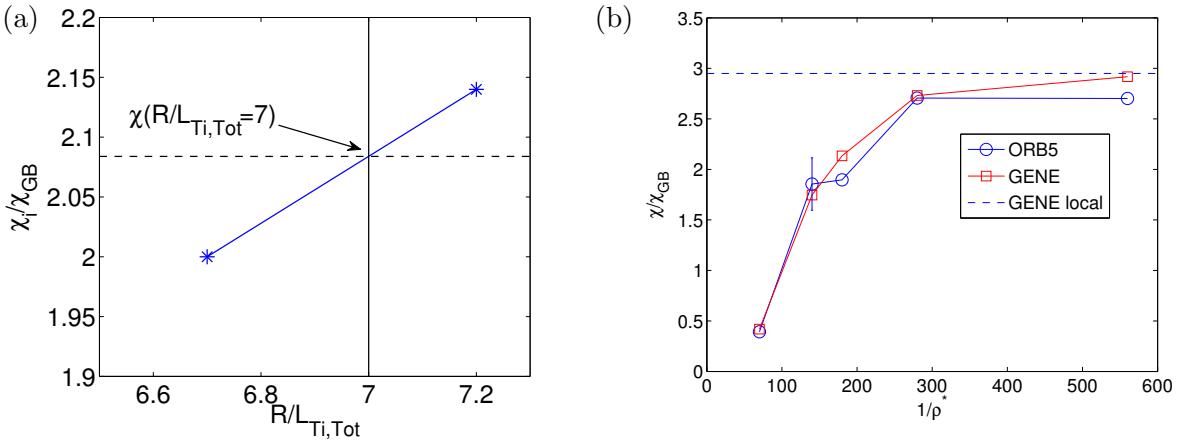

Figure 3. (a) The ion heat diffusivity for the nominal CBC logarithmic gradient $\kappa_T \approx 7$ is extracted using a linear interpolation of the time-averaged heat fluxes and gradients taken from two simulations with different initial temperature profiles. (b) Using this method, the GENE and ORB5 results are plotted for a series of ρ^* values and compared to the ion heat diffusivity of a local GENE simulation. The error bar at $\rho^* = 1/180$ is estimated using three ORB5 simulations with different initial conditions.

show excellent agreement though they are based on completely different numerical methods and are thus potentially subject to different types of discretization errors. Within the error bars, which have exemplarily been evaluated at $\rho^* = 1/180$ using three different initial conditions with ORB5, both codes approach the local GENE (flux tube) result at about $\rho^* \lesssim 1/500$ such that gyro-Bohm scaling would hold for large devices as ITER. Comparing with earlier results using similar parameters, the asymptotic value agrees quantitatively with the largest GTC run of Ref. [21]. Qualitatively, these results concur with the conclusion of Ref. [22] that the global results converge towards the local results in the $\rho^* \to 0$ limit. The exact value in the latter publication is interestingly quite close to the GENE result using an $\hat{s} - \alpha$ magnetic equilibrium model which differs in the treatment of small inverse aspect ratio terms [17]. Hence, the current investigations imply that small but decisive differences in the equilibrium models might be a very likely reason for earlier disagreement in ρ^* scalings. However, when comparing with experiments, it should be noted that profile shapes, for instance, might have a strong influence on the scaling as has already been observed above in linear investigations and in Ref. [20, 22]. More complete physics, e.g., a gyrokinetic treatment of electrons or electromagnetic fluctuations, might furthermore alter those results such that dedicated simulations are called for.

5. Avalanches in local and global simulations

As the anomalous transport scaling appears to be gyro-Bohm like at small ρ^* but non-gyro-Bohm like at $\rho^* \gtrsim 1/300$, the question as to which mechanisms are responsible for this transition arises. An often favored candidate are so-called avalanches, i.e. ballistically propagating structures in various observables as, for instance, in the heat fluxes [24, 25, 26]. The latter shall be considered

in the following. As can be seen in Fig. 4 such structures are indeed present in nonlocal, collisionless GENE simulations of adiabatic electron ITG modes using CBC-like parameters and they appear to be independent on whether a gradient or flux driven mode is chosen. Another

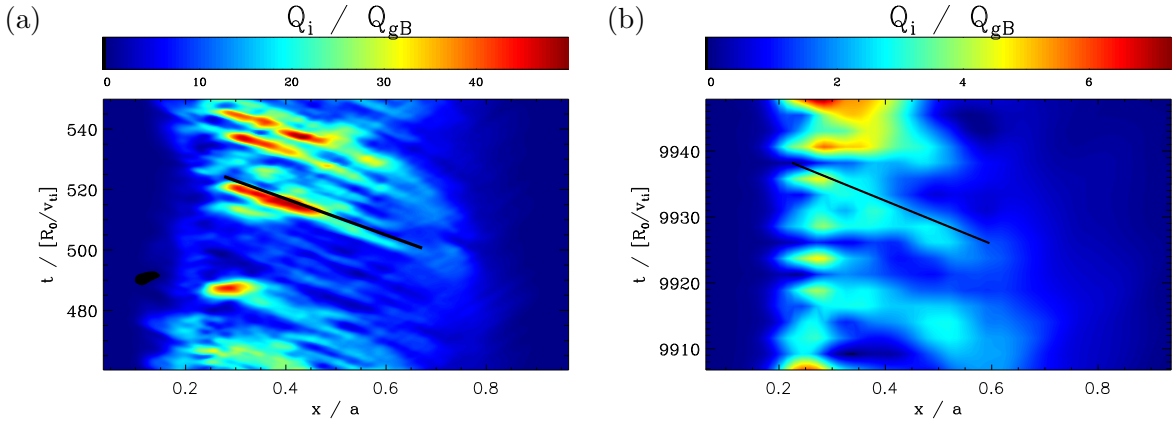

Figure 4. Flux surface averaged heat flux in units of $Q_{\mathrm{gB}} = p_0 c_s \rho_s^2 / R_0^2$ vs. time and radial coordinate. Plot (a) shows the result of a gradient driven simulation using the Krook type heat source at $\rho^* = 1/140$ while (b) contains the result of a low-resolution, "flux-driven" (by the localized physical heat source) simulation at $\rho^* = 1/80$. Black lines are added to emphasize the ballistic propagation of heat flux structures.

interesting feature is that both simulations being presented exhibit similar avalanche propagation velocities of about 2 in units of $\rho_s / R_0 c_s$ although they are performed at significantly different values of ρ^* and differing average temperature gradients – in the first case about $6.8 - 6.9$ while in the second about 6.6. For gradient driven simulations of adiabatic electron ITG modes, it has recently be stated that avalanches can be dominated by local physics instead of being governed (as often presumed) by global dynamics since characteristic avalanche parameters appeared to be closely correlated with the turbulent eddy space and time scales and not the machine size [26]. At least, for the simulations at hand the same argument seems to hold for flux-driven simulations. Based on these findings, avalanches should also be visible in local simulations. A corresponding result for the CBC parameters is shown in Fig. 5. Clearly, avalanche-like structures can be observed on this microscopic ($\rho^* \to 0$) scale, as well. However, due to the periodic boundary conditions and the constant temperature and density profiles, they do not exhibit a certain propagation direction but are restricted in their radial extent by large scale zonal flows, see Fig. 5(b). In line with the statements in Ref. [26], the avalanche propagation velocity is again close to $2\rho_s / R_0 c_s$ and corresponding radial correlation lengths being extracted by hand from Fig. 4(a) and Fig. 5 are very similar (about 105 and $85\rho_s$, respectively). Since in general, variations e.g. in the q-profile may affect particle orbits and wave-particle decorrelation physics, further investigations are required to determine the parameters space where the above findings still hold.

6. Conclusion

The new extension of the grid-based gyrokinetic turbulence code GENE by radial variations of the background profiles and metric coefficients has been introduced and tested for various linear and nonlinear scenarios. In this context, it was found that finite-size effects seem to be less important for large fusion devices, where gyro-Bohm scaling can be assumed for the given parameters. However, significant deviations from the local results are observed consistently at $\rho^* \gtrsim 1/300$ by two different gyrokinetic codes and explanations are provided why earlier studies appeared to be

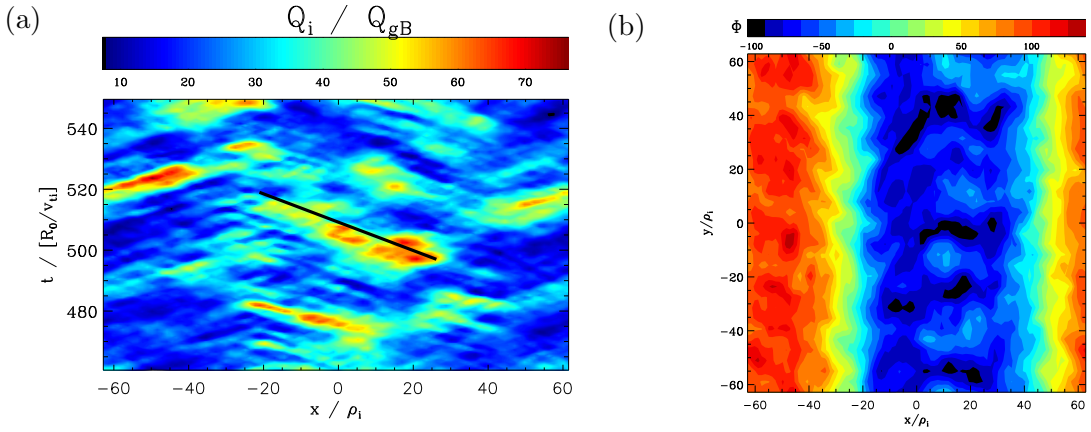

Figure 5. (a) Flux surface averaged heat flux vs. time and radial coordinate for a local GENE simulation using CBC parameters. The black line is added to emphasize the ballistic propagation of heat flux structures. (b) A snapshot ($t = 500\, R_0/c_s$) of the electrostatic potential at outboard midplane is shown to visualize the strong zonal flows which seem to "confine" the radial avalanche extent.

inconclusive. Heat flux avalanches have been investigated in three different scenarios and earlier claims on a (partially) local nature of these ballistically propagating structures are confirmed.

[1] Brizard A J and Hahm T S 2007 *Reviews of Modern Physics* **79** 421 (pages 48)
[2] Garbet X, Idomura Y, Villard L and Watanabe T H 2010 *Nuclear Fusion* **50** 043002
[3] Roberts K V and Taylor J B 1965 *Physics of Fluids* **8** 315–322
[4] Cowley S C, Kulsrud R M and Sudan R 1991 *Physics of Fluids B* **3** 2767–2782
[5] Beer M A, Cowley S C and Hammett G W 1995 *Phys. Plasmas* **2** 2687–2700
[6] Jenko F, Dorland W, Kotschenreuther M and Rogers B N 2000 *Phys. Plasmas* **7** 1904–1910
[7] Dannert T and Jenko F 2005 *Phys. Plasmas* **12** 072309
[8] Merz F 2008 *Gyrokinetic Simulation of Multimode Plasma Turbulence* Ph.D. thesis Westfälische Wilhelms-Universität Münster
[9] Görler T *et al* 2010 *J. Comput. Phys.* Submitted
[10] Jolliet S *et al* 2007 *Comput. Phys. Commun.* **177** 409–425
[11] McMillan B F, Jolliet S, Tran T M, Villard L, Bottino A and Angelino P 2008 *Phys. Plasmas* **15** 052308
[12] Candy J, Waltz R E, Parker S E and Chen Y 2006 *Phys. Plasmas* **13** 074501
[13] Idomura Y, Ida M, Tokuda S and Villard L 2007 *J. Comput. Phys.* **226** 244–262
[14] Jolliet S *et al* 2009 *Phys. Plasmas* **16** 072309
[15] Sarazin Y *et al* 2010 *Nucl. Fusion* **50** 054004
[16] Dimits A M *et al* 2000 *Phys. Plasmas* **7** 969–983
[17] Lapillonne X *et al* 2009 *Phys. Plasmas* **16** 032308
[18] Görler T 2009 *Multiscale Effects in Plasma Microturbulence* Ph.D. thesis Universität Ulm
[19] Villard L *et al* 2010 *Plasma Phys. Controlled Fusion* Accepted for publication
[20] McMillan B *et al* 2010 *Phys. Rev. Lett.* Accepted for publication
[21] Lin Z, Ethier S, Hahm T S and Tang W M 2002 *Phys. Rev. Lett.* **88** 195004
[22] Candy J, Waltz R E and Dorland W 2004 *Phys. Plasmas* **11** L25–L28
[23] Lapillonne X 2010 *Microturbulence in electron internal transport barriers in the TCV Tokamak and global effects* Ph.D. thesis École Polytechnique Fédérale de Lausanne
[24] Sarazin Y, Garbet X, Ghendrih P and Benkadda S 2000 *Phys. Plasmas* **7** 1085–1088
[25] Candy J and Waltz R E 2003 *J. Comput. Phys.* **186** 545–581
[26] McMillan B F *et al* 2009 *Phys. Plasmas* **16** 022310